International Journal of
Geo-Information

Article

Analysis of Hydrological Sensitivity for Flood Risk Assessment

Sanjay Kumar Sharma [1,*], Young-Joo Kwak [2,*], Rakesh Kumar [1] and Bibhash Sarma [3]

[1] National Institute of Hydrology, Centre for Flood Management Studies, Dispur, Assam 781-006, India; rakesh.nihr@gov.in
[2] International Centre for Water Hazard and Risk Management (ICHARM) under the auspices of UNESCO, Public Works Research Institute (PWRI), 1-6 Minamihara, Tsukuba, Ibaraki 305-8516, Japan
[3] Civil Engineering Department, Assam Engineering College, Guwahati 781-006, India; bsghy@yahoo.co.in
[*] Correspondences: sanjaypundit@gmail.com (S.K.S.); kwak@icharm.org (Y.-J.K.);
Tel.: +91-943-574-6774 (S.K.S.); +81-49-879-6779 (Y.-J.K.)

Received: 30 November 2017; Accepted: 1 February 2018; Published: 5 February 2018

Abstract: In order for the Indian government to maximize Integrated Water Resource Management (IWRM), the Brahmaputra River has played an important role in the undertaking of the Pilot Basin Study (PBS) due to the Brahmaputra River's annual regional flooding. The selected Kulsi River—a part of Brahmaputra sub-basin—experienced severe floods in 2007 and 2008. In this study, the Rainfall-Runoff-Inundation (RRI) hydrological model was used to simulate the recent historical flood in order to understand and improve the integrated flood risk management plan. The ultimate objective was to evaluate the sensitivity of hydrologic simulation using different Digital Elevation Model (DEM) resources, coupled with DEM smoothing techniques, with a particular focus on the comparison of river discharge and flood inundation extent. As a result, the sensitivity analysis showed that, among the input parameters, the RRI model is highly sensitive to Manning's roughness coefficient values for flood plains, followed by the source of the DEM, and then soil depth. After optimizing its parameters, the simulated inundation extent showed that the smoothing filter was more influential than its simulated discharge at the outlet. Finally, the calibrated and validated RRI model simulations agreed well with the observed discharge and the Moderate Imaging Spectroradiometer (MODIS)-detected flood extents.

Keywords: IWRM; flood risk; hydrological sensitivity; DEM; RRI model

---

1. Introduction

Integrated Water Resource Management (IWRM) was developed and increasingly recognized to meet urgent international and national demand for the effective and efficient management of water resources under climate change. In particular, transboundary river basins in Asia need to be managed in integrated ways that consider the interaction between flood risk reduction and sustainable development. According to the Technical Advisory Committee of Global Water Partnership [1], "IWRM is a process, which promotes the coordinated development and management of water, land and related resources in order to maximize the resultant economic and social welfare in an equitable manner without compromising the sustainability of vital ecosystems". Integrated flood risk management, in the context of IWRM, should take the highest priority in the international and regional development plans of both developing and developed countries. The holistic approach of IWRM should be complementary to mainstream disaster risk reduction and disaster management. This should be done in a planning process using a mathematical formula associated with scalable modules at the national, regional, and local levels under a socio-technical and institutional IWRM framework [2,3]. Keeping the importance of IWRM in view, the National Institute of Hydrology (NIH), a premier Indian institute in the area of hydrology and water resources, set up regional centers for conducting studies related to field problems and to develop a closer interaction with water resource management organizations across different regions of the country. One such regional center was set up at Guwahati, India for the northeastern region to tackle various water resource problems of seven northeast states, including Sikkim and parts of West Bengal. Under the mandate of the XII plan period, the center is working on a project in IWRM under the Pilot Basin Study (PBS).

The PBS program involves the identification of suitable basins in consultation with concerned state governments and authorities; the establishment of advanced instrumentation for data collection, storage, processing, and analysis using state of the art models; and the preparation of results and findings in collaboration with specialists of other relevant disciplines in a meaningful and usable form for intended beneficiaries and relevant stakeholders.

Most of the basins in Northeast India have insufficient hydrological gauge stations, so reliance on the availability of satellite products for hydrologic simulations is even greater. Elevation data from different sources are widely available, even for data-poor developing countries. Topography plays a major role in determining the accuracy of hydraulic modeling and flood inundation mapping [4,5]. Manfreda et al. (2008) investigated the topographic attributes of the terrain and observed a strong correlation between the topographic index and areas exposed to flood inundation [6–8]. The Digital Elevation Model (DEM) is a raster dataset containing the topographic information of a region and is used as a prerequisite to hydraulic modeling. Considerable variation is observed among different DEMs, depending on spatial resolution, vertical precision, and accuracy. This diversity is due to the types of equipment and methods used to obtain the topographic data. When DEMs are used as an input to hydraulic modeling, the differences in quality among them result in differences in model output performance [8]. To date, many studies have been carried out to evaluate the impact of topographic representation accuracy on the results of hydraulic models [9–12]. Patro et al. [13] selected a study area in India and demonstrated the usefulness of using the Shuttle Radar Topography Mission (SRTM) DEM to derive river cross-sections for use in hydraulic modeling. They found that the calibration and validation results from the hydraulic model performed quite satisfactorily in simulating river flow. Furthermore, the model performed quite well in simulating the peak flow, which is important in flood modeling. Tarekegn et al. [14] used a DEM generated from the ASTER image of a study area in Ethiopia. From the results obtained, they concluded that the ASTER DEM was able to simulate the observed flooding pattern and inundated area extents with reasonable accuracy. Paiva et al. [15] demonstrated the use of SRTM DEM in a large-scale hydrologic model with a full 1-D hydrodynamic module to calculate flow propagation on a complex river network. This study focused on different DEM sources from satellites—such as the Advanced Spaceborne Thermal Emission and Reflection Radiometer (ASTER), the Shuttle Radar Topography Mission (SRTM), and The Cartosat-1 Digital Elevation Model (CARTO DEM)—and their effect on flood simulation.

Objectives

The objective of this study was to evaluate the hydrological and topographical sensitivity of parameters for flood risk assessment based on the different conditions of the representative river basin. To determine the optimal parameters for hydrologic modeling, the Rainfall-Runoff-Inundation (RRI) model was employed to simulate and reproduce historical flood events in 2007 and 2008. Three different Digital Elevation Model (DEM) resources, i.e., ASTER, SRTM, and CARTO DEM, were modified by DEM smoothing techniques in pre-processing. They were then compared with a hydrologic simulation focusing on the comparison of river discharge and inundation area, specifically the maximum flood-peak discharge and maximum flood extent. Based on the three modified DEMs and optimal parameters from the experimental study basin, we sought common parameters reflected in the hydrological sensitivity characteristics of the Brahmaputra River Basin.

2. Study Area

The Kulsi River Basin, a part of the Brahmaputra sub-basin, was selected for the PBS study. The Kulsi River drains a total area of 2806 km^2, covering the Kamrup District of Assam, the Western Khasi Hills, and the Ri Bhoi District of Meghalaya in Northeast India. The selected basin is an ideal target to develop flood inundation maps due to its strategic location (encompassing two states in the northeast) and the fact that the region experiences large floods. The Kulsi River Basin is situated on the south bank of the mighty Brahmaputra River (Figure 1). It is located between latitude 25°30′ N to 26°10′ N and longitude 89°50′ E to 91°50′ E, with an altitude between 100 to 1900 m above mean sea level (AMSL). The area that the Kulsi River drains can be broadly divided into three reaches: (i) the Upper Khasi hill reach; (ii) the middle reserve forest reach; and (iii) the alluvial or flood plain reach.

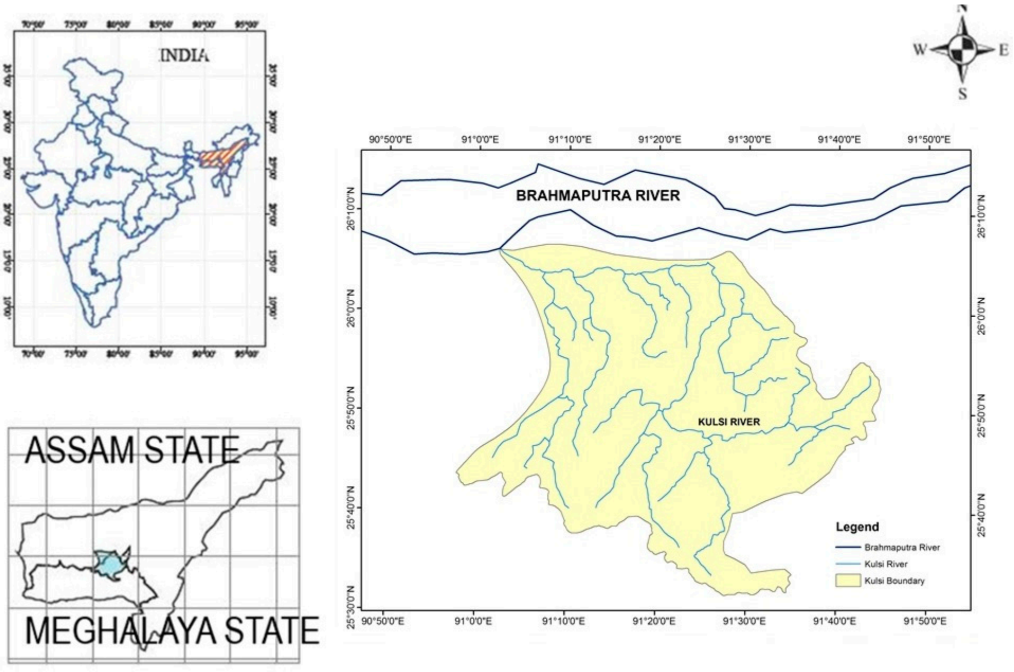

Figure 1. Location of the Kulsi River Basin.

2.1. Data

The daily rainfall data from 2007 and 2008 were provided by the Indian Meteorological Department and were collected from five rain gauges in and around the Kulsi River Basin (Figure 2). The daily discharge data at the outlet for 2007 and 2008 were collected from the Centre Water Commission of India. Information on the outlet and boundary of the Kulsi River Basin were obtained from the Centre Water Commission of India.

Three DEMs were used in this study to characterize the topography of the study area. HYDROlogical data and maps based on SHuttle Elevation Derivatives at multiple Scales (HYDROSHEDS) were comprised of high-resolution processed elevation data at 90 m spatial resolution; this was obtained from a space shuttle flight for NASA's Shuttle Radar Topography Mission (SRTM). The ASTER DEM ver. 2 maintains the Geotiff format with a 30 m spatial resolution. The data was downloaded for the study from the ASTER GDEM distribution website developed by the Ministry of Economy, Trade, and Industry of Japan (METI) and the National Aeronautics and Space Administration (NASA) [16]. CARTO DEM is a national DEM developed by the Indian Space Research Organisation (ISRO) that is derived from the Cartosat-1 stereo payload launched in May 2005. The primary output unit is a tile of 7.5′ by 7.5′ in size with a DEM spacing of 1/3 arc-sec (with 10 m spatial resolution). The data products were downloaded from National Remote Sensing ISRO (NRSC) [17].

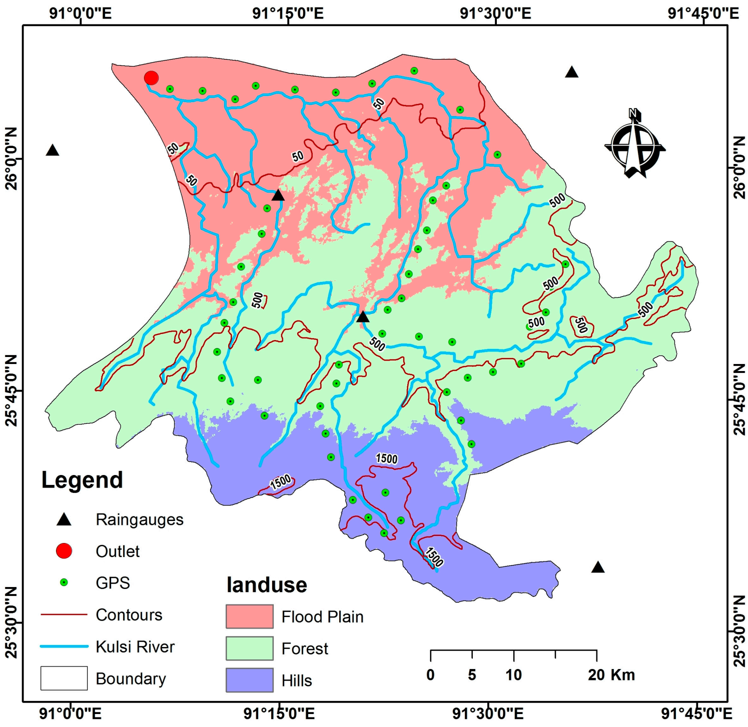

Figure 2. Location of rain gauges, GPS stations, and discharge site.

The soil data for the study was obtained from the Harmonized World Soil Database v 1.2 of the Food and Agriculture Organization (FAO) soil portal. The Harmonized World Soil Database is a 30 arc-second raster database. The soil data for the study area was downloaded from the FAO [18]. The soil texture of the Kulsi River Basin consists of sandy loam (29%), sandy clay (25%), and clay loam (46%). Elevation values were measured at fifty locations along the Kulsi River (Figure 2) using the Differential Global Positioning System (DGPS).

To validate the inundation area on 13 June, 2008, the Moderate Resolution Imaging Spectroradiometer (MODIS) eight-day composite surface reflectance products (MYD09A1 from the Aqua satellite platform) were used to detect floodwater between 9 and 16 June 2008. The data product was downloaded from the Land Processes Distributed Active Archive Centre, US Geological Survey (USGS) [19].

2.2. Methods

The RRI model is a 2D model capable of simultaneously simulating rainfall-runoff and flood inundation [20,21]. The flow on the slope grid cells is calculated with a 2D diffusive wave model, while the channel flow is calculated with a 1D diffusive wave model. The vertical infiltration flow is estimated using the Green-Ampt model. The Green-Ampt infiltration model is the most widely used model and is built into the RRI Model.

The RRI model was used to model hydrological behaviour in the study area. The details of the model are shown below. The model equations are derived from the following mass balance equation and momentum equation for a gradually varied unsteady flow:

$$\frac{\partial h}{\partial t} + \frac{\partial q_x}{\partial x} + \frac{\partial q_y}{\partial y} = r - f \tag{1}$$

$$\frac{\partial q_x}{\partial t} + \frac{\partial u q_x}{\partial x} + \frac{\partial v q_x}{\partial y} = -gh\frac{\partial H}{\partial x} - \frac{\tau_x}{\rho_w} \tag{2}$$

$$\frac{\partial q_y}{\partial t} + \frac{\partial u q_y}{\partial x} + \frac{\partial v q_y}{\partial y} = -gh\frac{\partial H}{\partial y} - \frac{\tau_y}{\rho_w} \tag{3}$$

where:

- h = height of the water from the local surface,
- q_x, q_y = unit width discharges in x and y directions,
- u, v = flow velocity in x and y directions,
- r = rainfall intensity,
- f = infiltration rate,
- H = height of the water from the datum,
- ρ_w = density of water,
- g = gravitational acceleration, and
- τ_x, τ_y = shear stress in x and y directions.

The second terms on the right side of Equations (2) and (3) are calculated with the Manning's equation:

$$\frac{\tau_x}{\rho_w} = \frac{gn^2 u\sqrt{u^2+v^2}}{h^{1/3}} \tag{4}$$

$$\frac{\tau_y}{\rho_w} = \frac{gn^2 v\sqrt{u^2+v^2}}{h^{1/3}} \tag{5}$$

where n is the Manning's roughness parameter.

The RRI model spatially discretizes the mass balance (Equation (1)) as follows:

$$\frac{dh^{i,j}}{dt} + \frac{{q_x}^{i,j-1} - {q_x}^{i,j}}{\Delta x} + \frac{{q_y}^{i,j-1} - {q_y}^{i,j}}{\Delta y} = r^{i,j} - f^{i,j} \tag{6}$$

where ${q_x}^{i,j}, {q_y}^{i,j}$ are x and y direction discharges from a grid cell at (i, j), respectively.

Equations (7) and (9) describe the saturated subsurface flow and Equations (8) and (10) describe the combination of the saturated subsurface flow and the surface flow based on the Darcy law. For the kinematic wave model, the hydraulic gradient is assumed from the topographic slope, and the RRI model assumes the water surface slope as the hydraulic gradient:

$$q_x = -k_a h\frac{\partial H}{\partial x}(h \le d) \tag{7}$$

$$q_x = -\frac{1}{n}(h-d_a)^{5/3}\sqrt{\left|\frac{\partial H}{\partial x}\right|}sgn\left(\frac{\partial H}{\partial x}\right) - k_a(h-d_a)\frac{\partial H}{\partial x}(d_a < h) \tag{8}$$

$$q_y = -k_a h\frac{\partial H}{\partial y}(h \le d) \tag{9}$$

$$q_y = -\frac{1}{n}(h-d_a)^{5/3}\sqrt{\left|\frac{\partial H}{\partial y}\right|}sgn\left(\frac{\partial H}{\partial y}\right) - k_a(h-d_a)\frac{\partial H}{\partial y}(d_a < h) \tag{10}$$

where k_a is the lateral saturated hydraulic conductivity and d_a is the soil depth multiplied by the effective porosity.

Equation (11) is used to simulate the effect of unsaturated subsurface flows, saturated subsurface flows, and the surface flow with the single variable of h:

$$q_x = \begin{cases} -k_m d_m \left(\frac{h}{d_m}\right)^{\beta} \frac{\partial H}{\partial x}, & (h \le d_m) \\ -k_a (h - d_m) \frac{\partial H}{\partial x} - k_m d_m \frac{\partial H}{\partial x}, & (d_m < h \le d_a) \\ -\frac{1}{n} (h - d_a)^{5/3} \sqrt{\left|\frac{\partial H}{\partial x}\right|} sgn\left(\frac{\partial H}{\partial x}\right) - k_a (h - d_m) \frac{\partial H}{\partial x} - k_m d_m \frac{\partial H}{\partial x}, & (d_a < h) \end{cases} \tag{11}$$

DEM products are sometimes created and distributed without any correction to the height obtained from data acquisition or processing for errors caused by artefacts and trees. DEM smoothing is an important pre-processing step to remove such errors. The main purpose of the smoothing algorithm is to remove certain high-frequency information in DEMs, while preserving genuine information at all frequencies [22,23]. Based on the advantages and disadvantages of several DEM smoothing algorithms, three algorithms, i.e., low-pass filter, enhanced lee filter, and denoising algorithms, were selected to remove noise from SRTM, ASTER, and CARTO DEMs. These simple and fast smoothing algorithms remove noise effectively while clearly preserving the mesh features (i.e., sharp edges and corners) of these three DEMs on flood inundation simulations.

A low-pass filter, known as a blurring or smoothing filter, averages the rapid changes in an image. It calculates the average value of pixels in a window and all of its eight intermediate neighbours. The result replaces the original value of the pixel. The process is repeated for every pixel in the image. The equation to calculate the enhanced Lee filter is given below:

$$\mathrm{Y_{ij}} = \mathrm{K^0} + \mathrm{W} \times (\mathrm{C} - \mathrm{K^0}) \tag{12}$$

where $\mathrm{Y_{ij}}$ is the despeckled image, $\mathrm{K^0}$ is the mean of the kernel/window, W is the weight factor, and C is the centre element in the kernel/window. The denoising algorithm based on [22] works by iteratively filtering the face normals by the weighted averages of neighbouring face normals and, then, updating the vertex positions to correspond with denoised face normals.

The topographic data consisting of SRTM, ASTER, and CARTO DEMs were processed using the Hydrology toolset for the ArcGIS Spatial Analyst extension (ESRI, CA, USA) because DEMs usually consist of undesired errors, classified as sinks or peaks. A sink is an area surrounded by higher elevation values, while a peak is defined as an area surrounded by lower elevation values. More accurate DEMs, called depressionless DEMs, create more accurate flow directions and accumulated flows after all errors (such as sinks and peaks) are removed. In this study, depressionless DEMs were created using a fill sink tool of the Hydrology toolset. Then, flow direction and flow accumulation were computed from the three types of depressionless DEMs. The RRI model, a subroutine of DemAdjust2.exe, was employed to further correct the values of flow direction and accumulation from depressionless DEMs. Elevation, flow direction, and flow accumulation grids were exported in the ASCII format for use as input in the RRI model.

Rainfall–runoff data corresponding to a flood event observed in the study area during 2007 was used for calibrating the RRI model. The RRI model was set up to simulate the flow of the Kulsi River at the outlet. The calibration of the RRI model was done by matching the simulated hydrograph with the observed hydrograph of the 2007 flood. The sensitivity check scenarios were performed with RRI input parameters to assess their influence on the hydrologic simulation. The validation of the RRI model was performed by executing the model with the parameters calibrated to the 2008 flood event.

Remote sensing images from the Moderate Imaging Spectroradiometer (MODIS) were used to determine the flood inundation extent in the Kulsi River Basin. The Modified Land Surface Water

Index (MLSWI) was used to identify flooded areas [24,25]. MLSWI was calculated using Equation (13) as follows:

$$\text{MLSWI} = \frac{1 - R_{NIR} - R_{SWIR}}{1 - R_{NIR} + R_{SWIR}} \tag{13}$$

where *NIR* stands for near infrared reflectance and SWIR for shortwave infrared reflectance. R_{NIR} and R_{SWIR} are the reflectance values (R) of MODIS bands 2 and 7, respectively. An optimal threshold of the MLSWI was selected as 0.64 in order to discriminate water bodies from other land-cover features based on their spectral characteristics. The flood extent, determined by the MLSWI, was used to evaluate the accuracy of simulated results attained using the RRI model based on the different DEMs, with and without smoothing.

To verify the correspondence between RRI-based and MODIS-detected flood areas, the Critical Success Index (CSI) was used as categorical verification statistic. CSI is computed using the following formula:

$$CSI = \frac{RRI_{area} \cap MODIS_{area}}{RRI_{area} \cup MODIS_{area}} \tag{14}$$

A perfect simulation using categorical verification statistics would have a CSI value of 1.

3. Results

3.1. Topographic Data Processing

The processed depressionless DEMs of SRTM, ASTER, and CARTO were obtained as shown in Figure 3. On visual inspection, all the DEMs exhibited similar trends in the spatial distribution of specified elevation ranges, with exceptions for the lowest and highest elevation values.

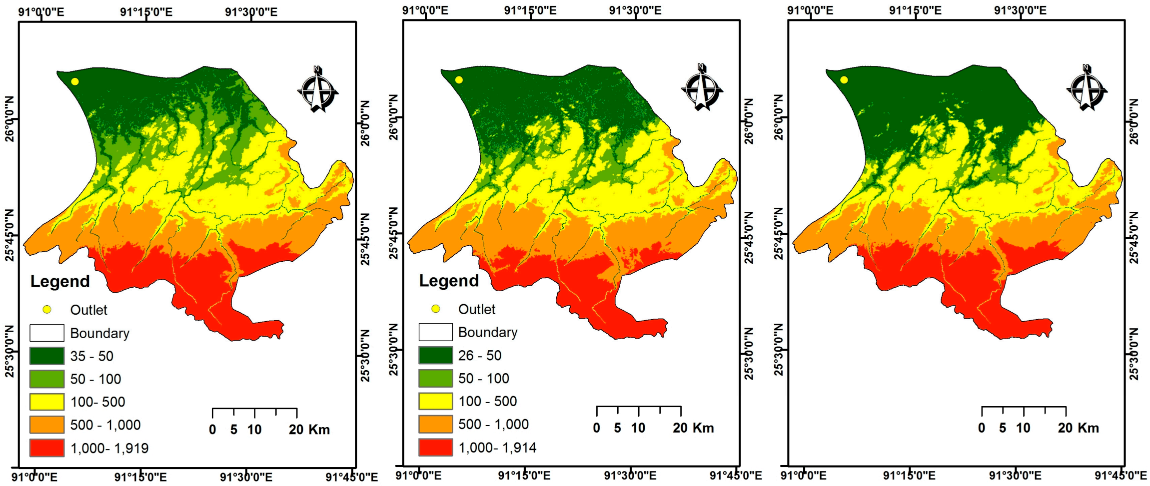

Figure 3. Depressionless Digital Elevation Models (DEM) used in the study.

Table 1 shows the basic statistics derived from the processed DEM. The maximum elevation was observed in the CARTO DEM, followed by the SRTM and ASTER DEMs. The highest mean elevation was observed in the SRTM DEM, and the highest standard deviation was observed in ASTER.

Table 1. Characteristics of depressionless DEMs.

Basic Statistics	SRTM	ASTER	CARTO
Minimum elevation (m)	35.0	26.0	33.0
Maximum elevation (m)	1919.0	1914.0	1926.0
Mean elevation (m)	869.1	833.5	852.7
Standard deviation	539.6	551.6	541.3

To determine the accuracy of DEMs, 50 ground-based elevations represented by the DGPS measurements were compared with the elevations in SRTM, ASTER, and CARTO DEM. The DGPS measurements were classified into two categories: one consisting of the DGPS values located in the flood plains, and the other consisting of the DGPS values located in the forests and hilly areas. Figure 4 compares the three DEM sources with the DGPS in the elevation of flood plains.

To quantify the differences in elevation between the DGPS points and the DEM data, root-mean-square error (RMSE) and mean absolute error (MAE) values were computed for the flood plains and for the forests and hills in the study area, as shown in Table 2.

Table 2. Comparison of elevations in the three DEMs (i.e., Advanced Spaceborne Thermal Emission and Reflection Radiometer (ASTER), Shuttle Radar Topography Mission (SRTM), and Cartosat-1 (CARTO)) and the Differential Global Positioning System (DGPS).

Source of DEM	Flood Plains		Forests and Hills	
	RMSE (m)	MAE (m)	RMSE (m)	MAE (m)
SRTM	1.88	1.73	9.53	8.82
ASTER	3.85	3.15	6.95	5.94
CARTO	8.08	7.08	8.81	10.46

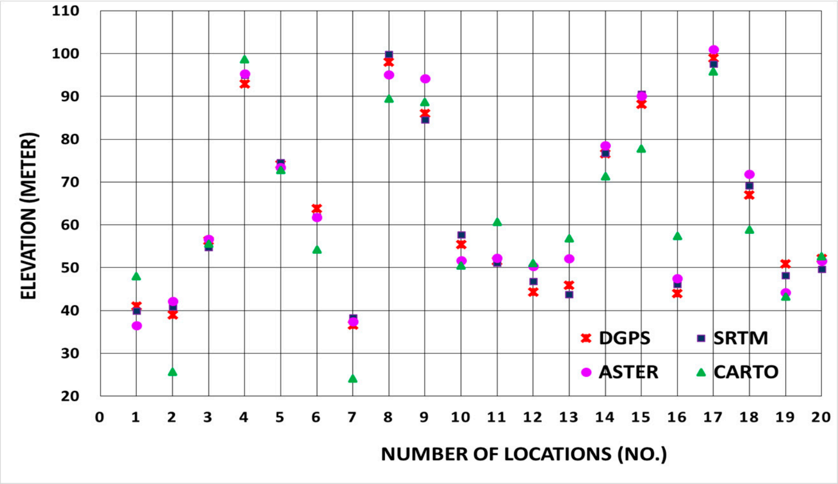

Figure 4. Comparison of elevation of the DGPS points with elevation of the SRTM, ASTER, and CARTO DEM points for flood plains.

The computed error analysis found that the SRTM DEM produced the lowest RMSE and MAE for the flood plains, i.e., 1.88 m and 1.73 m, respectively; however, for the remaining study area, the best results for RMSE and MAE were obtained from the ASTER DEM, i.e., 6.95 m and 5.94 m, respectively.

Figure 5 shows the DEM-derived slopes from three depressionless DEMs. According to the visual interpretation of the slope maps, the overall slope values modified by SRTM DEM were higher than both the ASTER and CARTO DEMs in the flood plain. The higher slope values signify that a slope will accelerate a velocity of water flow in the basin as a primary driving component in any hydrologic model. Therefore, the simulated peak discharge will be produced by a steep slope regulating runoff behaviour. The differences in the slope values and the spatial distribution consequently lead to differences in the hydrologic response.

The watersheds, which were delineated using the flow directions derived from different DEMs, also displayed differences in spatial extent (Figure 6), especially near the outlet of the basin. Watershed areas of 24,846.5, 25,017.6, and 25,187.7 km^2 were obtained using the SRTM, ASTER, and CARTO DEMs, respectively.

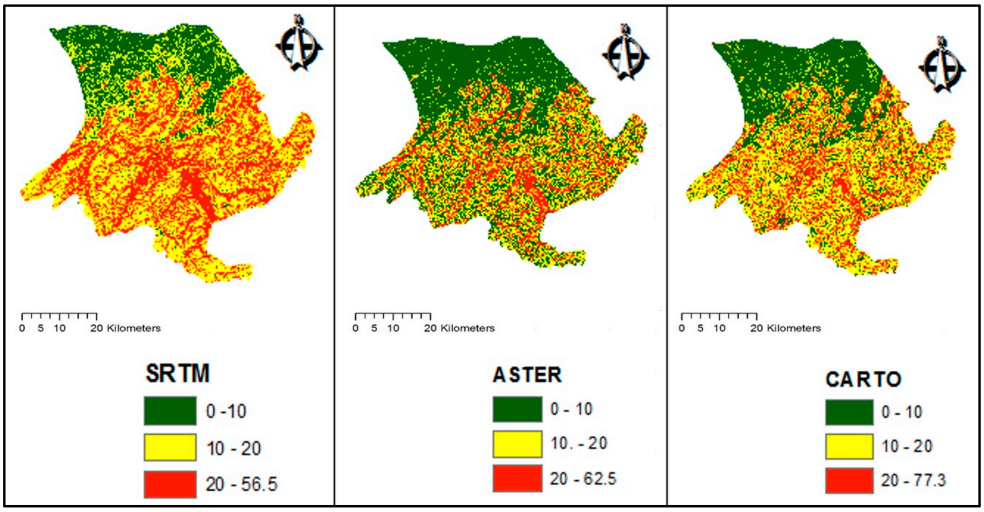

Figure 5. DEM-derived slopes in the study.

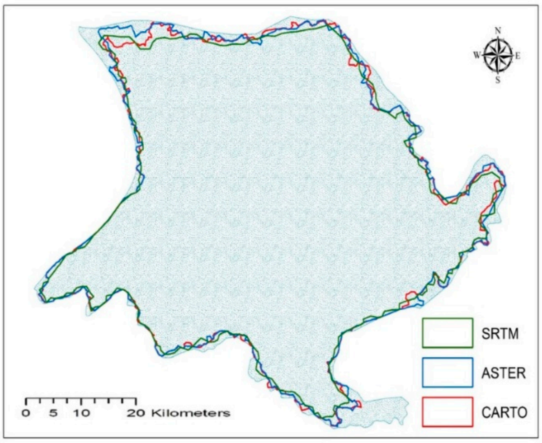

Figure 6. Comparison of delineated watersheds obtained using three different DEMs.

3.2. Sensitivity Analysis of Manning's Roughness Coefficient in Hydrologic Simulation

Manning's n values were set to those between the highest and lowest values prescribed by the RRI manual. This was in order to evaluate the impact of Manning's roughness coefficient on the discharge and inundation area simulated by the RRI model. This section discusses the impact of different Manning's n values on hydrologic simulations using different DEMs.

Figure 7a shows the RRI model variation in simulated discharge caused by changing n from 0.15 to 1.0. The best fit of simulated values compared to the observed discharge value was given when $n = 0.4$. The figure clearly shows that decreases in the Manning's n values resulted in increases in discharge, and vice versa. Flood flow peaks showed higher rates of change compared to the observed discharge values (the blue dotted line) due to the variation in Manning's n value. In general, a 5% decrease in Manning's n value resulted in an increase in flood peak by 3.35%.

Figure 7b shows the RRI model variation in simulated discharge caused by changing n from 0.15 to 1.0 for ASTER DEM. Change trends in flood peak when using ASTER DEM was similar to the previous case. In general, a 5% decrease in the Manning's *n* value resulted in an increase in flood peak by 2.05%.

Figure 7c shows the RRI model variation in simulated discharge caused by changing *n* from 0.15 to 1.0 in the CARTO DEM. In this case, a 5% decrease in values resulted in an increase in flood peak by 2.73%. Among the DEMs used in this study, the SRTM DEM exhibited the highest sensitivity to changes in the Manning's *n* value, followed by the ASTER and CARTO DEMs.

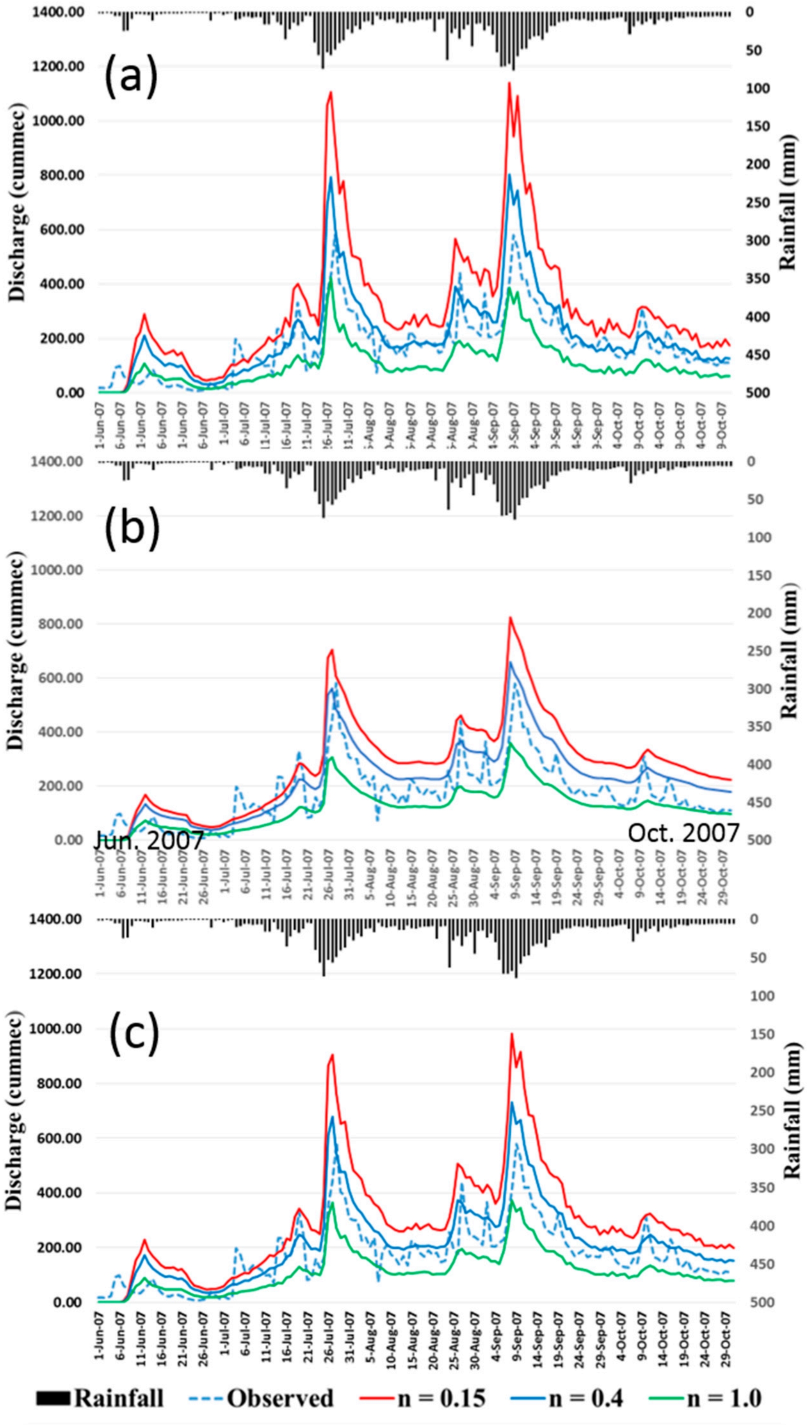

Figure 7. Sensitivity to the Manning's *n* values in (**a**) SRTM DEM; (**b**) ASTER DEM; and (**c**) CARTO DEM based on the discharge at the outlet.

3.3. Sensitivity Analysis of Soil Depth in Hydrologic Simulation

After fixing the Manning's *n* values, the soil depth parameter in the RRI model was varied based on the specifications of the RRI manual. The soil type selected was clay, as it yielded the best RRI model performance out of all the soil types. The value of soil depth ranged from d = 0.5–2.0 m, and the effect of soil depth on the hydrologic simulation was estimated. The differences between the model simulations and observed discharge could be attributed to the fact that a single soil type was selected, despite there being different soil types in the study basin. The following section discusses the sensitivity of RRI model simulations using different DEMs to soil depth.

Figure 8a shows the RRI model variation in simulated discharge caused by changing the soil depth from the lowest value of d = 0.15 m to the best-fitting value of d = 1.5, then, to the highest recommended value of d = 2.0 m. From the figure, the general trend is that a decrease in d value results in an increase in discharge. The range of the variation in flood peaks was lower than that of the peak variation observed in relation to changing the Manning's *n* value, which suggests that discharge values were less sensitive to soil depth than to the Manning's *n* value.

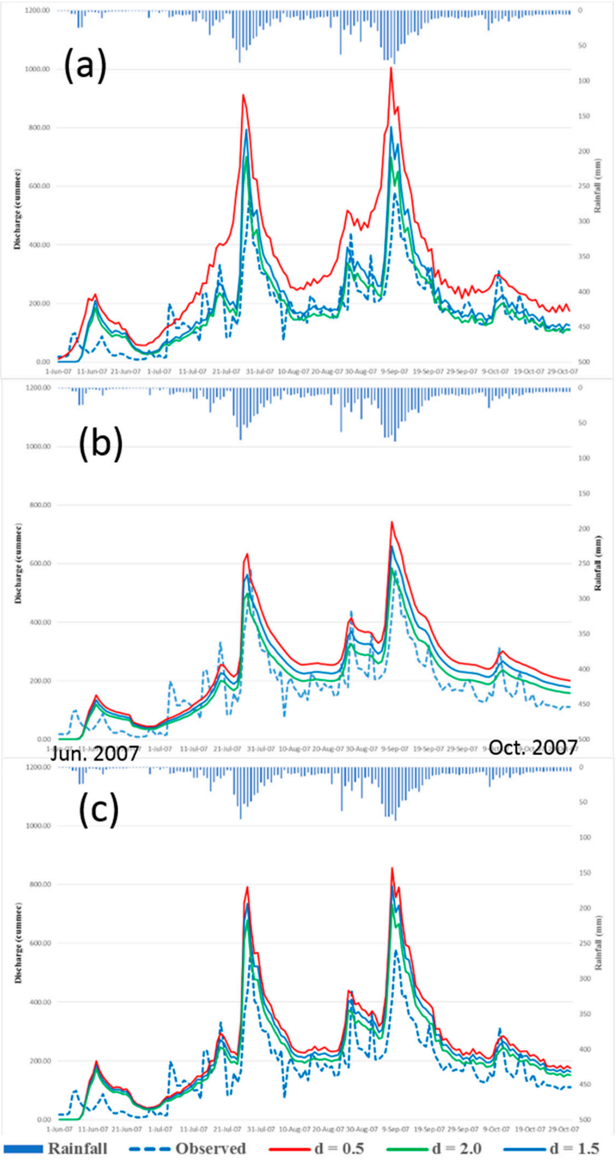

Figure 8. Sensitivity to soil depth values in (**a**) SRTM DEM, (**b**) ASTER DEM, and (**c**) CARTO DEM based on the discharge at the outlet.

Figure 8b shows the RRI model variation in simulated discharge caused by changing soil depth values. Changing the values of soil depth by 5% resulted in a 1.7% change in discharge peaks in the ASTER DEM. The maximum flood peaks were quite similar among all the soil depth values; however, the intermediate peaks were not well simulated, which indicates possible limitations of the data or the RRI model used in this study.

Figure 8c shows the RRI model variation in simulated discharge caused by changing soil depth values in the CARTO DEM. Changing the values of soil depth by 5% resulted in a 0.6% change in discharge peaks in the CARTO DEM.

3.4. Sensitivity Analysis of Smoothing of Different DEMs on Hydrologic Simulation

After calibrating the RRI model with the Manning's *n* values and the soil depth parameter, the effect of different smoothing filters of DEMs on the hydrologic simulation was observed. Four types of filters, i.e., low-pass filter, enhanced Lee filter (window size = 3), enhanced Lee filter (window size = 5), and denoising algorithms, were applied to SRTM, ASTER, and CARTO DEMs. The following section discusses the sensitivity of different DEMs to smoothing filters using the RRI model simulation.

Figure 9a shows the RRI model variation in simulated discharge caused by using different smoothing filters for SRTM DEM. The use of a low-pass filter generally resulted in the simulation of higher discharge values. The denoising algorithm resulted in the lowest discharge values and were closer to the observed discharge values (the blue dotted line) in the hydrograph.

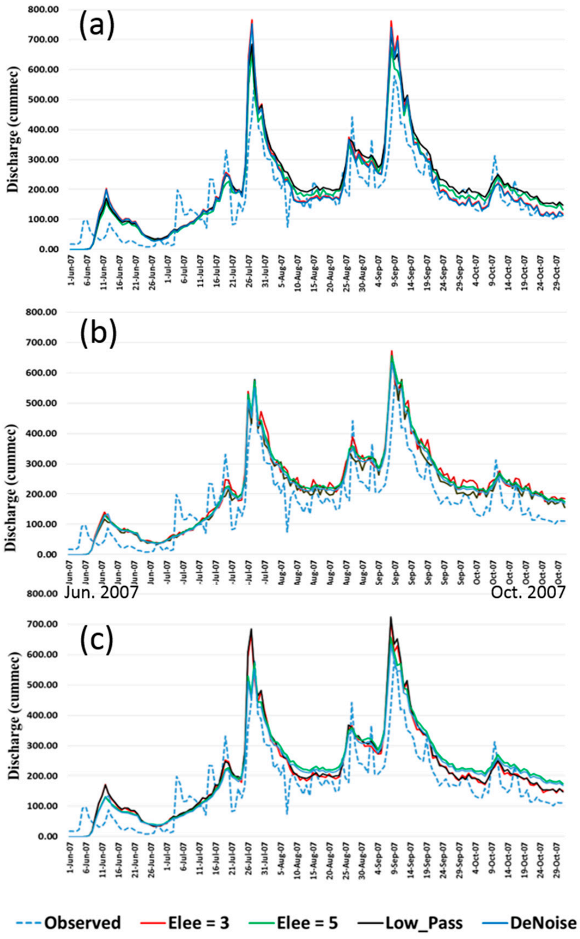

Figure 9. Sensitivity to smoothing in (**a**) SRTM DEM. (**b**) ASTER DEM, and (**c**) CARTO DEM based on the discharge at the outlet.

Figure 9b shows the RRI model variation in simulated discharge caused by using different smoothing filters in ASTER DEM. The simulation with a low-pass filter generally resulted in lower discharge values. The enhanced Lee filter with a size 3 × 3 window produced the highest peak and variation of the simulated discharge. The use of a denoising algorithm resulted in the lowest discharge values, which were closer to the observed discharge values (the blue dotted line) in the hydrograph.

Figure 9c shows the RRI model variation in simulated discharge caused by using different smoothing filters in CARTO DEM. The low-pass filter generally resulted in the simulation of higher discharge values for the major peaks, while the enhanced Lee filter with a 5 × 5 window resulted in higher discharge values for the intermediate peaks. The denoising algorithm resulted in simulating the lowest discharge values, which were closer to the observed hydrograph.

3.5. Simulation of Flood Extent Using the Rainfall-Runoff-Inundation (RRI) Model

The inundation area on 13 June 2008 was computed using RRI models and DEMs, with and without smoothing. The results were compared with the MLSWI derived from MODIS imagery. Table 3 shows the comparison of the inundation area simulated by the RRI models using different DEMs. The inundation area derived from the MODIS imagery on the same date was calculated as 560.09 km^2.

Table 3. Comparison of simulated flood extent using the Moderate Imaging Spectroradiometer (MODIS) imagery for the 2008 flood.

Source of DEM	Inundation Area (km^2)				
	Without Smoothing	Low Pass Filter	Lee Filter (Size = 3)	Lee Filter (Size = 5)	Denoising Algorithm
SRTM	310.76	279.66	262.20	260.69	364.18
ASTER	433.83	377.13	431.03	442.94	450.95
CARTO	348.68	306.21	382.36	304.41	366.25
Source of DEM	**CSI**				
	Without Smoothing	**Low Pass Filter**	**Lee Filter (Size = 3)**	**Lee Filter (Size = 5)**	**Denoising Algorithm**
SRTM	0.45	0.31	0.28	0.28	0.47
ASTER	0.47	0.41	0.46	0.49	0.57
CARTO	0.44	0.33	0.42	0.32	0.51

A comparison of the inundation area showed that the area simulated by the RRI model using ASTER DEM was closer to the area derived using the MODIS imagery. The CSI between the RRI model and the MODIS imagery produced values of 0.45, 0.47, and 0.44 for SRTM, ASTER, and CARTO DEMs, respectively. The combination of the denoising algorithm and ASTER DEM produced an inundation area of 450.95 km^2 and a CSI of 0.57, which was closest to the flood extent derived using the MODIS imagery.

Figure 10 shows a comparison in the spatial distributions of the flooded areas of the flood plain. It compares the areas simulated by the best performing combination of ASTER DEM and the denoising algorithm using the RRI model (the blue and light blue pixels) with the areas detected by MODIS using the MLSWI algorithm (the blue and red pixels). Maximum inundation was observed around the river confluences and near the outlet in the flood plains. To verify the maximum inundation areas, we visited representative flood plain sites near the river mouth of the Kulsi River on June 2017. We further conducted a field investigation to collect ground truth information using a small unmanned aerial vehicle (sUAV: MAVIC Pro quadcopter with a flight control system, DJI Technology Co. Ltd., Shenzhen, China), which is useful for flood monitoring using less labour and time. The location of the sUAV flight control was around 91°6′42.12″ E, 26°4′41.52″ N near the river mouth of the Kulsi River. The sUAV, which achieved a flight altitude of 30 m and a radius of 80 m, successfully captured the micro-topographic features of flood inundation, i.e., the conditions of floodwater over a two-meter water depth, submerged roads, and flooded rice fields near the outlet. Despite the different severities (based on magnitude, return period, duration, and extent of flooding) of the floods in 2007, 2008, and 2017, the water level in 2017 exceeded the flood danger level in the Brahmaputra River, particularly in the Assam State of India. However, the 2017 flooding caused no less damage to the area (due to river flood and bank erosion) than the 2007 and 2008 floods. We found that the sUAV-captured inundated areas represented both the RRI-simulated and MLSWI-detected inundation areas.

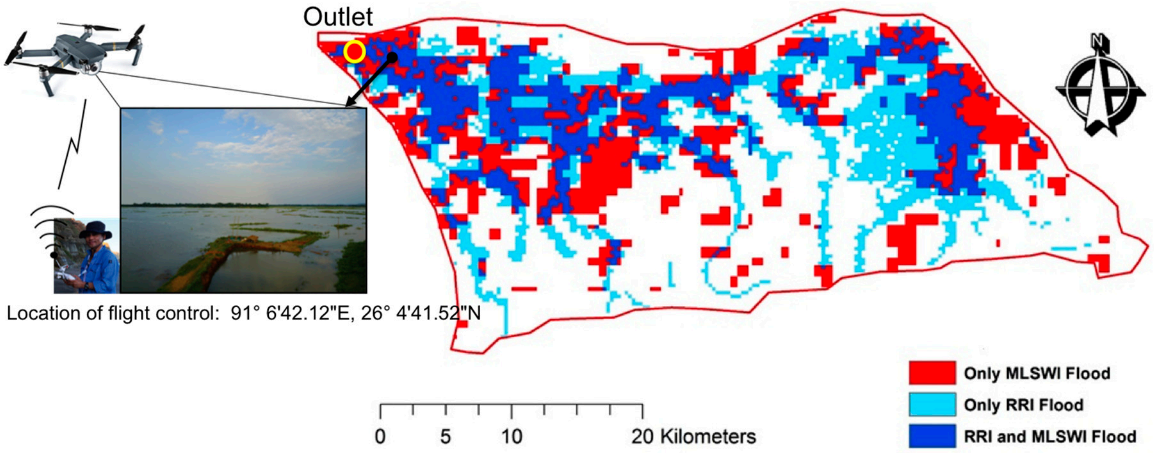

Figure 10. Resultant inundation areas. (**a**) Comparison of the best performing Rainfall-Runoff-Inundation (RRI) model (ASTER DEM with the denoising algorithm) with the MODIS-detected extent by the Modified Land Surface Water Index (MLSWI). (**b**) Field investigation using a small unmanned aerial vehicle (sUAV).

4. Discussion

Flood disasters need to be addressed in the context of IWRM. The overall framework of IWRM must balance the losses caused by inundation of the flood plains with the benefits of preserving the ecosystem and its associated biodiversity. Structural measures for land and water management must be integrated in the delineated flood inundated areas. Based on the results of this study, the importance of hydrological sensitivity in the case of regional flood inundation is discussed. In this study, two types of flood simulations in 2007 and 2008, using geomorphological conditions reproduced by the RRI model, were conducted to evaluate their effects on hydrological simulations of flood discharge and inundation area. The calibrated and validated RRI model reproduced the maximum flood inundation in order to analyse hydrological sensitivity based on discharge. This helps gain a comprehensive understanding of regional floods in Northeastern India.

First, the remarkable variations among the different DEMs were revealed by the topographic characteristics of the Kulsi River Basin. The quality of topographic data is dependent on several factors, including sampling density, data acquisition, spatial resolution, the interpolation algorithms used to generate a DEM, and terrain characteristics, as also reported in [26]. The determination of the absolute accuracy of DEMs, based on DGPS measurements, can be well explained by the different surface patterns of low-lying areas and the gentle and steep slopes in the forest and hill areas of the basin. The presence of thick forests along the gently rolling topography of the basin might have increased the errors of the DEM due to the backscattering of signals from different satellite sensors; this was more prominently seen in the SRTM DEM in this study. Among the DEMs used in this study, the SRTM DEM identified the smallest watershed area as the hydrological boundary condition of the basin. This tendency was reproduced in the RRI simulations of flood inundation extent using the SRTM DEM. When compared to ASTER and CARTO DEMs, the raw SRTM data with moderate resolution (90 m) was less capable of capturing the variation in flow direction, especially near the outlet of the basin.

Checking the influence of discharge at the upstream points of the basin, and not only at the outlet point, would increase the reliability of the RRI simulation.

Although the absolute vertical accuracy of DEMs was evaluated in this study, the comparison of the relative elevation accuracy of DEMs using high-resolution topographic maps would also be useful in determining their suitability for hydrologic simulation. High-resolution DEM data with a 5 m spatial resolution is available from the Advanced Land Observing Satellite (ALOS), operated by the Japan Aerospace Exploration Agency (JAXA). ASTER DEM outperformed the SRTM and CARTO DEMs in simulating the flood extent in this study. This finding is supported by the study undertaken by Tarekegn et al. [14] in Ethiopia using a DEM generated from ASTER images, where integration between remote sensing and GIS techniques was needed to construct flood plain terrain and channel bathymetry. From the results obtained, they concluded that ASTER DEM was able to simulate the observed flooding pattern and inundated area extents with reasonable accuracy. Nevertheless, they also highlighted the need for advanced GIS geoprocessing knowledge when developing a digital representation of the flood plain and channel terrain.

Second, we found that the selection of smoothing algorithms had a serious influence on the hydrologic simulations using different DEMs. For optimal speckle reduction, we also applied a spatial filter to each pixel with different window sizes, i.e., an enhanced Lee filter. The enhanced Lee filter with a 3 × 3 window performed RRI simulation better than one with a 5 × 5 window. Improving the best-fitting parameters of smoothing filters for hydrological simulations of different resolutions will be useful in determining the best-fitting parameters required to adequately characterize catchment behaviour. The inclusion of evapotranspiration, river cross-section data, base flow, and the interaction of ground water with surface water will also enhance the performance and reliability of the RRI model. Variation in soil depth also produced different flood simulation results, which was validated by the observed soil depth; Rahimy [27] has already studied the effect of soil depth spatial variation on runoff simulations.

Third, the simulation of flood extent by the RRI model was consistent along the river network, while MODIS imagery displayed patchy inundation areas. The reason for this could be attributed to the low spatial resolution of MODIS imagery and the limitations of MODIS in the presence of mixed areas within the pixel. This could also be because of the limitations of the index adopted to differentiate flood and non-flood areas. A comparison of the flood inundated area with multi-temporal SAR and optical images should improve the reliability of the RRI model simulation; for example, using TerraSAR-X (X-band, 1~3 m, DLR), Sentinel-1B (C-band, 5 m, ESA), ALOS-2 (L-band, 3 m, JAXA), WorldView-4 (0.3 m, GeoEye, USA), and Landsat-8 (15 m, USGS, USA).

Finally, in future works, an uncertainty analysis of topography DEMs using Monte Carlo simulations will be beneficial in quantifying the impact of using different topographical data on RRI model simulation. Different flood simulation models, such as the Hydrologic Modelling System (HEC-HMS, U.S. Army Corps of Engineers) and MIKE HYDRO River (MIKE 11 and 21, DHI), should be tested using different sources in order to compare the hydrological sensitivity of the discharge and inundation areas based on the selected parameters. In addition, in line with the improvement of a project in IWRM under the Pilot Basin Study (PBS), we would like to expand the pilot area by applying an improved approach for integrated flood risk management. We would like to do this with particular reference to the Brahmaputra River of the Assam District, North East India, as well as to the whole of the Brahmaputra River Basin as an international-level transboundary river.

5. Conclusions

The following conclusions were drawn from the study: (1) compared to the reference points of DGPS measurements, SRTM DEM produced the fewest errors in the flood plains, while the relatively good accuracy of the DEM was obtained from ASTER DEM for the forests and hills; (2) the sensitivity analysis revealed that the RRI model for flood plains was most sensitive to Manning's n values compared with the other input parameters, followed by the sources (original products) of DEMs and soil depth; (3) calibration and validation of the RRI model reproduced the maximum flood-peak discharge quite well; (4) the simulated inundation extent was more influenced by topography-modified smoothing filters than its simulated discharge at the outlet of the basin; and (5) the denoising algorithm performed better than the other DEM smoothing filters in hydrological simulations.

Acknowledgments: This research was supported by the Japan Society for the Promotion of Science (JSPS) KAKENHI Grant-in-Aid for Scientific Research B: 15H05136.

Author Contributions: Young-Joo Kwak led this research and designed the whole study as the principal investigator of Grant B: 15H05136. Sanjay K. Sharma contributed to perform all the processes and in analysing the data to develop a flood inundation map using satellite data and the RRI model. Rakesh Kumar and Bibhash Sarma coordinated this research.

Conflicts of Interest: The authors declare no conflict of interest.

References

1. Global Water Partnership. *Integrated Water Resource Management (IWRM) at a Glance: Technical Advisory Committee*; Global Water Partnership Secretariat: Stockholm, Sweden, 2000.
2. UNESCO. *Introduction of the Integrated Water Resources Management (IWRM) Guidelines at River Basin Level*; UN-World Water Assessment Programme (WWAP): Paris, France, 2009; 39p.
3. UNEP. *The UN-Water Status Report on the Application of Integrated Approaches to Water Resources Management*; UNEP: Nairobi, Kenya, 2012; 106p.
4. Sanders, B.F. Evaluation of on-line DEMs for flood inundation modeling. *Adv. Water Resour.* **2007**, *30*, 1831–1843. [CrossRef]
5. Cook, A.; Merwade, V. Effect of topographic data, geometric configuration and modeling approach on flood inundation mapping. *J. Hydrol.* **2009**, *377*, 131–142. [CrossRef]
6. Manfreda, S.; Sole, A.; Fiorentino, M. Can the basin morphology alone provide an insight into floodplain delineation. *WIT Trans. Ecol. Environ.* **2008**, *118*, 47–56.
7. Kirkby, M.J. *Hydrograph Modeling Strategies*; Department of Geography, University of Leeds: Leeds, UK, 1975.
8. Vaze, J.; Teng, J.; Spencer, G. Impact of DEM accuracy and resolution on topographic indices. *Environ. Model. Softw.* **2010**, *25*, 1086–1098. [CrossRef]
9. Cobby, D.M.; Mason, D.C.; Davenport, I.J. Image processing of airborne scanning laser altimetry data for improved river flood modeling. *ISPRS J. Photogramm. Remote Sens.* **1999**, *56*, 121–138. [CrossRef]
10. Casas, A.; Benito, G.; Thorndycraft, V.R.; Rico, M. The topographic data source of digital terrain models as a key element in the accuracy of hydraulic flood modeling. *Earth Surf. Process. Landf.* **2006**, *31*, 444–456. [CrossRef]
11. Schumann, G.; Matgen, P.; Cutler, M.E.J.; Black, A.; Hoffmann, L.; Pfister, L. Comparison of remotely sensed water stages from LiDAR, topographic contours and SRTM. *ISPRS J. Photogramm. Remote Sens.* **2008**, *63*, 283–296. [CrossRef]
12. Kwak, Y.; Takeuchi, K.; Fukami, J.; Magome, J. A new approach to flood risk assessment in Asia-Pacific region based on MRI-AGCM outputs. *Hydrol. Res. Lett.* **2012**, *6*, 55–60. [CrossRef]
13. Patro, S.; Chatterjee, C.; Mohanty, S.; Singh, R.; Raghuwanshi, N.S. Flood inundation modeling using MIKE FLOOD and remote sensing data. *J. Indian Soc. Remote Sen.* **2009**, *37*, 107–118. [CrossRef]
14. Tarekegn, T.H.; Haile, A.T.; Rientjes, T.; Reggiani, P.; Alkema, D. Assessment of an ASTER-generated DEM for 2D hydrodynamic flood modeling. *Int. J. Appl. Earth Observ. Geoinf.* **2010**, *12*, 457–465. [CrossRef]
15. Paiva, R.C.; Collischonn, W.; Tucci, C.E. Large scale hydrologic and hydrodynamic modeling using limited data and a GIS based approach. *J. Hydrol.* **2011**, *406*, 170–181. [CrossRef]
16. The Ministry of Economy, Trade and Industry of Japan (METI) and the National Aeronautics and Space Administration (NASA), ASTER Global Digital Elevation Model (ASTER GDEM). Available online: http://www.jspacesystems.or.jp/ersdac/GDEM/E/index.html (accessed on 10 January 2015).
17. National Remote Sensing Indian Space Research Organisation (NRSC). Available online: http://www.nrsc.gov.in/ (accessed on 10 January 2015).
18. Food and Agriculture Organization of the United Nations (FAO). Harmonized World Soil Database v 1.2. Available online: http://www.fao.org/soils-portal/soil-survey/soil-maps-and-databases/harmonized-world-soil-database-v12/en/ (accessed on 10 January 2015).

19. Land Processes Distributed Active Archive Center. US Geological Survey Land Processes Distributed Active Archive Center. Available online: https://lpdaac.usgs.gov/ (accessed on 20 May 2015).
20. Sayama, T.; Ozawa, G.; Kawakami, T.; Nabesaka, S.; Fukami, K. Rainfall–runoff–inundation analysis of the 2010 Pakistan flood in the Kabul River basin. *Hydrol. Sci. J.* **2012**, *57*, 298–312. [CrossRef]
21. Sayama, T.; Tatebe, Y.; Iwami, Y.; Tanaka, S. Hydrologic sensitivity of flood runoff and inundation: 2011 Thailand floods in the Chao Phraya River basin. *Nat. Hazards Earth Syst. Sci.* **2015**, *15*, 1617–1630. [CrossRef]
22. Sun, X.; Rosin, P.L.; Martin, R.R.; Langbein, F.C. Fast and effective feature-preserving mesh denoising. *IEEE Trans. Vis. Comput. Graphics* **2007**, *13*, 925–938. [CrossRef] [PubMed]
23. Lee, J.S. Refined filtering of image noise using local statistics. *Comput. Graphics Image Process.* **1981**, *15*, 380–389. [CrossRef]
24. Kwak, Y.; Arifuzzanman, B.; Iwami, Y. Prompt proxy mapping of flood damaged rice fields using MODIS-derived indices. *Remote Sens.* **2015**, *7*, 15969–15988. [CrossRef]
25. Kwak, Y. Nationwide Flood Monitoring for Disaster Risk Reduction Using Multiple Satellite Data. *ISPRS Int. J. Geo-Inf.* **2017**, *6*, 203. [CrossRef]
26. Sharma, K.; Saraf, A.K.; Das, J.D.; Rawat, V.; Shujat, Y. SRTM and ASTER DEM characteristics of two areas from Himalayan region. *Int. Geoinf. Res. Dev. J.* **2010**, *1*, 25–31.
27. Rahimy, P. Effects of soil depth spatial variation on runoff simulation using the Limburg Soil Erosion Model (LISEM), a case Study in Faucon Catchment, France. *Soil Water Res.* **2012**, *7*, 52–63.